


ORIGINAL ARTICLE

Polarization switching dynamics and switchable diode effect in hybrid improper ferroelectric $\text{Ca}_3\text{Ti}_2\text{O}_7$ ceramics

Bao Y. Tong¹ | Shou Yu Wang^{1,2}  | Winnie Wong-Ng² | Xiongnan Zhang³ | Cong Huang³ | Hui Zhao¹ | Weifang Liu^{2,3}

¹College of Physics and Material Science, Tianjin International Joint Research Centre of Surface Technology for Energy Storage Materials, Tianjin Normal University, Tianjin, China

²Materials Measurement Science Division, National Institute of Standards and Technology, Gaithersburg, Maryland

³Tianjin Key Laboratory of Low Dimensional Materials Physics and Preparing Technology, School of Science, Tianjin University, Tianjin, China

Correspondence

Shou Yu Wang, College of Physics and Material Science, Tianjin International Joint Research Centre of Surface Technology for Energy Storage Materials, Tianjin Normal University, Tianjin, China. Email: sywang@tjnu.edu.cn
 Weifang Liu, Tianjin Key Laboratory of Low Dimensional Materials Physics and Preparing Technology, School of Science, Tianjin University, Tianjin, China. Email: wfliu@tju.edu.cn

Funding information

National Key Research and Development Program of China, Grant/Award Number: 2018YFB0703500; National Natural Science Foundation of China, Grant/Award Number: 51572193; Natural Science Foundation of Tianjin, Grant/Award Number: No. 17JCYBJC17600

Abstract

Hybrid improper ferroelectric $\text{Ca}_3\text{Ti}_2\text{O}_7$ (CTO) ceramics were synthesized by a solid-state reaction method. Their polarization switching currents, dynamic processes of polarization-switching, and leakage current properties were investigated. It was found that the dynamic polarization curves of CTO ceramics exhibit obvious dependence on the frequency of the driving electric fields. Moreover, CTO ceramics show a switchable diode effect. The underlying mechanism for the observed effects were proposed based on the interplaying between mobile charged defects and bound charges. The charged defects also lead to a decrease in the band gap of the CTO ceramic, as revealed by absorption spectrum analysis.

KEYWORDS

$\text{Ca}_3\text{Ti}_2\text{O}_7$, ceramic, ferroelectric polarization, hybrid improper ferroelectric, switchable diode effect

1 | INTRODUCTION

Multiferroic materials that simultaneously exhibit ferroelectric and magnetic orderings have attracted great interests due to their potential applications in spintronic and photocatalytic devices, data storage, and sensors.^{1–3} BiFeO_3 and BaTiO_3 are typical examples of conventional ferroelectrics,

in which electric polarization is considered as the order parameter characterizing the structure phase transition from high-temperature prototypic to low-temperature ferroelectric state.⁴ It is universally acknowledged that BiFeO_3 is still the only single-phase room-temperature multiferroic material. Recently, magnetoelectric coupling were obviously observed in $\text{Bi}_{3.25}\text{La}_{0.75}\text{Ti}_{2.5}\text{Nb}_{0.25}(\text{Fe}_{0.5}\text{Co}_{0.5})_{0.25}\text{O}_{12}$

ceramic by Li et al via composition modification.⁵ In recent years, significant attention has been paid to the study of the hybrid improper ferroelectricity (HIF). Benedek et al were the first to introduce the term HIF to describe a state where the electric polarization is induced by a complex distortion pattern consisting of octahedral rotation mode and octahedral tilt mode.⁶ Bousquet et al reported that a electric polarization can also arise from the coupling of two rotational modes in certain ABO_3 perovskite superlattices.⁷ Because the spontaneous electric polarization in those materials is not the primary order parameter anymore in the structure phase transition, they are called “improper” ferroelectrics.⁸ Such a concept paves an avenue for the research of room-temperature multiferroic materials with possible magnetoelectric coupling via modulating the octahedral tilt and rotation by electric field.

$\text{Ca}_3\text{Mn}_2\text{O}_7$ and $\text{Ca}_3\text{Ti}_2\text{O}_7$ (CTO) may indeed be good candidates for research on HIFs. A rich set interesting physical properties has been predicted in $\text{Ca}_3\text{Mn}_2\text{O}_7$ such as ferroelectricity, magnetoelectricity, and weak ferromagnetism induced by oxygen octahedral rotations.⁶ CTO is a member of the $\text{Ca}_{n+1}\text{Ti}_n\text{O}_{3n+1}$ family with $n = 2$. In recent years, several studies have been reported on electrical, optical, and structural properties of CTO. Benedek et al investigated the lattice dynamical properties of CTO using first-principles theoretical calculations and predicted that CTO may exhibit an electric polarization of $20 \mu\text{C}/\text{cm}^2$.⁹ Yoon et al provided the first experimental evidence of ferroelectric polarization and ferroelastic domain structure at room temperature in single-crystal samples of $\text{Ca}_{3-x}\text{Sr}_x\text{Ti}_2\text{O}_7$ ($x = 0, 0.54$, and 0.85).¹⁰ Moreover, optical spectroscopy and band gap analysis of single crystals CTO samples have been investigated through theoretically calculation and experimental verification.¹¹ Nowadnick et al used group theory methods and first-principles calculations to investigate the possible ferroelectric switching pathway in CTO with low-energy barriers via an orthorhombic twin domain, an antipolar stacking domain, or a rhombohedral-like phase.¹² In a report by Huang et al, the high-energy antiphase boundaries and ferroelastic tilting and rotation domain walls were found to dominate the nucleation controlled kinetics of polarization flipping in a CTO single crystal.¹³ Very recently, employing pulsed laser deposition, Li et al deposited CTO thin films onto SrTiO_3 single-crystal substrates and found that CTO film exhibits a coercive field of $5 \text{ kV}/\text{cm}$ at a temperature of 2 K . While the coercive field of bulk CTO single crystal is around $120 \text{ kV}/\text{cm}$.¹⁴ The remnant polarization values of CTO have been reported to be 8 ,¹⁰ 0.6 ,⁸ and $8 \mu\text{C}/\text{cm}^2$ ¹⁴ for single crystal along the $[100]$ direction, ceramic and thin film, respectively. Furthermore, those polarization characteristics were all probed and extracted from the so-called positive-up-negative-down (PUND) process. In this method, with applying the double triangular waveform voltage to

measure the polarization vs electric field (P - E) hysteresis loops, the influence of the nonpolar contribution from leakage current could be removed. However, the dynamic hysteresis measurement result was not reported until now, although dynamic hysteresis probing allows a comprehensive investigation of the characteristics in the P - E hysteresis loop within a wide frequency range. In addition, the influence of leakage current through the ferroelectric layer would be included in the dynamics hysteresis loop. It is known that the leakage current can strongly deteriorate the ferroelectric polarization and electrical reliability. Until now, the electric transport properties and dynamic hysteresis loops including the effect of leakage current on CTO ceramics have not been reported.

In this paper, highly resistive CTO ceramics were characterized to illustrate the contribution of ferroelectric domain switching to current vs biased electric field (I - E) curves. The effect of leakage current on ferroelectric behavior was investigated by a combination of dynamic hysteresis loops and PUND analysis. We also presented the switchable diode effect in CTO ceramics and discussed the possible mechanism for the observed switching resistance. We further report our investigation of the optical band gap of CTO ceramics.

2 | EXPERIMENTAL PROCEDURE

$\text{Ca}_3\text{Ti}_2\text{O}_7$ ceramics were synthesized by a conventional solid-state reaction method in air. Stoichiometric mixtures of high purity CaCO_3 (99.99%), TiO_2 (99.99%) were thoroughly grounded for 10 hours in agate mortars with alcohol and preheated at 1000°C for 10 hours. After preheating, the calcined powder was hydrostatically cold pressed into 0.2 mm thick disks for 300 seconds under a uniaxial pressure of 30 MPa and sintered at 1450°C for 48 hours in air. Dense CTO ceramics were obtained after natural cooling to room temperature.

Analysis of the CTO's crystalline structure was carried out with X-ray diffraction using D/MAX-2500 diffractometer with Cu-K_α radiation (Rigaku Co., Tokyo, Japan)* and using the Rietveld structure refinement. For the morphological study, scanning electron microscopy was done using field-emission scanning electron microscope with model SU8010 series (Hitachi Co., Tokyo, Japan). For the measurement of electrical properties, both surfaces of ceramic disks were polished and coated with silver paste as electrodes. Ferroelectric polarization (P - E) and leakage current (J - E) vs electric field were recorded using a ferroelectric

*The purpose of identifying the equipment in this article is to specify the experimental procedure. Such identification does not imply recommendation or endorsement by the National Institute of Standards and Technology.

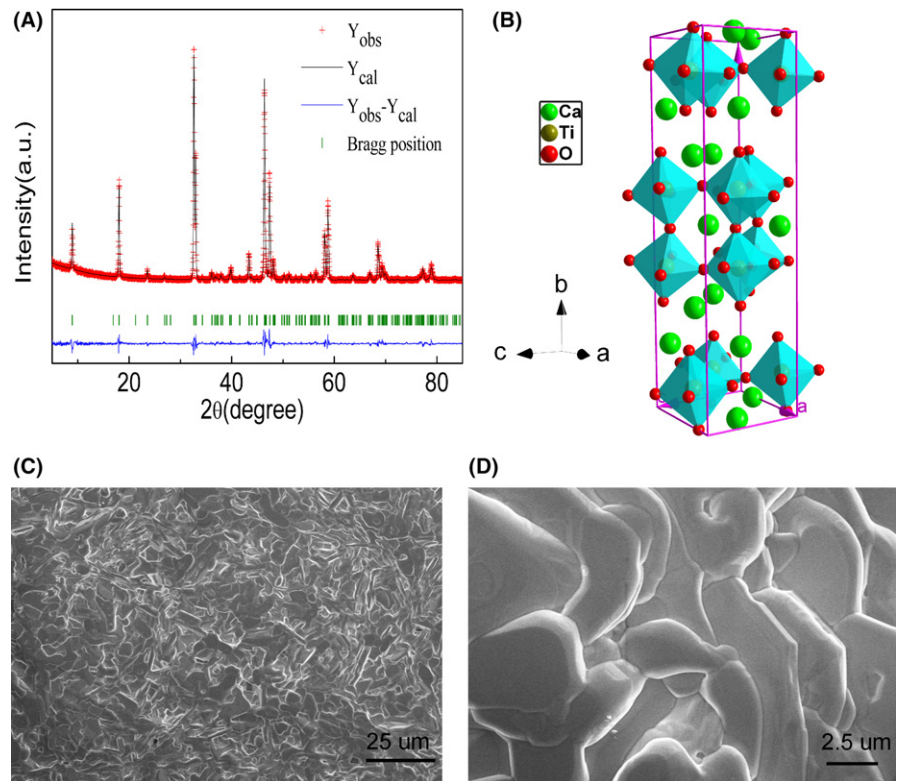


FIGURE 1 A, Rietveld-refined XRD pattern of CTO ceramic at room temperature. B, Crystal structure of CTO with the $Ccm2_1$ space group. C and D, SEM images of CTO ceramics with magnifications of $\times 800$ and $\times 6000$, respectively. [Color figure can be viewed at wileyonlinelibrary.com]

analyzer (Axiacct model TF2000; aixPES Co., Aachen, Germany). X-ray photoelectron spectroscopy (XPS) was performed with a PHI1600 spectrometer (Ulvac-Phi Co., Chigasaki, Kanagawa, Japan) to analyze the chemical states of the constituents. UV-vis absorption spectra were recorded with a UV-3600 UV-VIS-NIR spectrophotometer (Shimadzu Co., Tokyo, Japan).

3 | RESULTS AND DISCUSSION

The Rietveld refined XRD patterns of CTO ceramic is shown in Figure 1A, which indicates that all main XRD diffraction peaks could be well fitted with a single-phase $Ccm2_1$ model. The crystal structure of CTO, which is a distorted perovskite with strongly distorted TiO_6 octahedrons, is schematically shown in Figure 1B. The CTO unit cell is composed with two $CaTiO_3$ perovskite blocks layers and a CaO layer alternating with each other along the b axis.⁹ The Rietveld refinements yielded a good fit and no additional diffraction peaks exist in the measured XRD profile, which indicates that no impurity phases are present in the CTO sample. The final refined lattice parameters are $a = 5.4095(8) \text{ \AA}$, $b = 19.5167(9) \text{ \AA}$, $c = 5.4107(6) \text{ \AA}$, and $V = 571.26 \text{ \AA}^3$. The lattice volume is slightly larger than that reported in literature (570.46 \AA^3).¹⁵ Typical SEM images of the CTO grains are shown in Figure 1C and D. It is observed that the distribution of grain size is

homogeneous, and porosity seldom exists among the compact connected grains in CTO ceramics. The shapes of most grains are flaky.

Figure 2A shows loops of ferroelectric polarization vs electric field (P - E) as measured with positive up negative down (PUND) method at room temperature with electrical fields up to 175 kV/cm . It can be seen that all hysteresis loops show rectangular shape, indicating a ferroelectric nature in present CTO ceramics. With a maximum electrical field of 175 kV/cm , the coercive field and remnant polarization of the CTO ceramic are about 113 kV/cm , and $0.78 \text{ } \mu\text{C/cm}^2$, respectively. These values are comparable to the reported results.⁸ Since the PUND method has already removed the influence of nonhysteresis components on the P - E loop, in order to observe the effect of leakage current on the P - E loop, the dynamic P - E and I - E loops were probed. It is worth noting that the dynamic hysteresis loop (Figure 2C-E) is different from P - E loop with PUND method (Figure 2A). In these P - E loops obtained by two different measurement methods, the coercive field and the remnant polarization cannot be directly compared. Because dynamic P - E loop cannot reflect the true polarization flipping process of the ferroelectric domain, the coercive field mentioned below (Figure 2C-E) is defined as electric field at which the current peak appears on the I - E loop.

Figure 2B shows dynamic loops of switching current vs electric field under various maximum driving electric fields (E_m) for CTO. The E_m of the triangle wave used for the

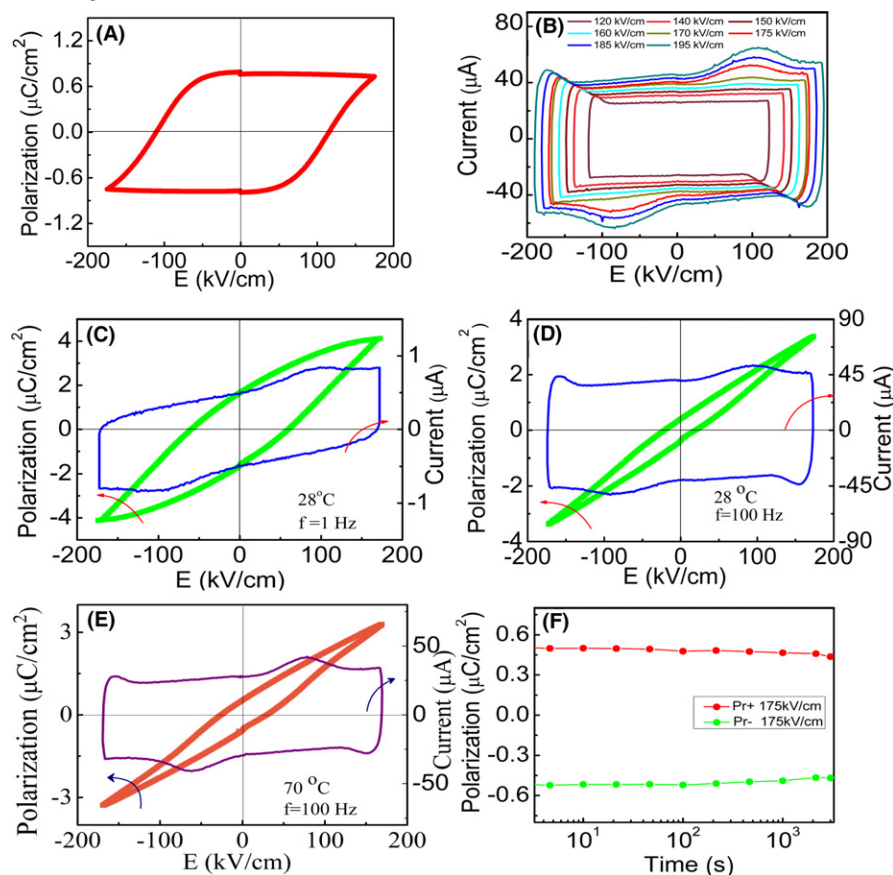


FIGURE 2 A, *P-E* hysteresis loops of CTO ceramic obtained by PUND measurement. B, Loops of polarization switching current vs electric field (*I-E*) under various maximum driving electric fields for CTO. C and D, *I-E* and *P-E* loops as measured at frequency of 1 and 100 Hz, respectively, at 28°C. E, The *I-E* and *P-E* loops for CTO ceramic measured at 100 Hz at 70°C. F, Polarization retention of CTO ceramics.[Color figure can be viewed at wileyonlinelibrary.com]

measurements of switching currents was from 120 to 195 kV/cm. When $E_m > 150$ kV/cm, the polarization switching current start to show a bump at around 100 kV/cm, which indicates the reversion of the ferroelectric domains in CTO ceramics. The current peak position increases and shifts slightly towards higher electric field with the increase in E_m . It is known that an applied electric field can lead to an obvious change of the surface charges in the samples. One contribution of the surface charge is the switching of ferroelectric dipoles that is manifested by a peak in the switching current curve. If the resistance of the CTO sample is not high enough, the leakage currents passing through the CTO bulk will be large and overlay the current of ferroelectric dipoles switching. In this case, the peak from the switching current would disappear. Hence, the observed switching current peaks shown in Figure 2B indicate high resistance of CTO ceramics.

Figure 2C and D show the dynamic *I-E* and *P-E* loops of CTO ceramics with electrical field up to 175 kV/cm at frequency of 1, and 100 Hz, respectively. The larger peak-current value at higher frequency can be attributed to the higher switching rate of the electric field.¹⁶ The values of intersection with the vertical axis of CTO ceramics are 1.73, and 0.39 $\mu\text{C}/\text{cm}^2$ at frequency of 1, and 100 Hz, respectively. The corresponding value of intersection with the horizontal axis is 100 and 22 kV/cm. The increasing

rounded shape and the remnant polarization in *P-E* loops with decreasing measuring frequency is a result of the contribution from the leakage current. When increasing the temperature to 70°C the leakage current density will be dramatically enhanced (that will be discussed in next section), leading to a larger value 0.5 $\mu\text{C}/\text{cm}^2$ of intersection with the vertical axis and a smaller value of intersection with the horizontal axis, as shown in Figure 2E. The lower density of leakage current is important to attain excellent retention properties for ferroelectric capacitor. Figure 2F presents the retention characteristics of the remnant polarization of the CTO capacitor after poling with 175 kV/cm. It is found that there is no obvious degradation for remnant polarization even after 3000 seconds.

Figure 3A-C show the room-temperature leakage current density vs electric field (*J-E*) curves for the CTO sample in the bias range of ± 80 , ± 110 , and ± 170 kV/cm, respectively. We can see from Figure 3A that, in measurement process, the electrical field which biased the top electrode was swept from $0 \rightarrow +80 \rightarrow 0 \rightarrow -80 \rightarrow 0$ kV/cm, as denoted by the numbers labeled in that figure. *J-E* characteristics on a semi-logarithmic scale are also plotted in the inset of Figure 4A. The *J-E* curves in Figure 3A are almost symmetric from 10^{-8} to 10^{-6} A/cm² and show only weak hysteresis behavior. When sweeping electrical field was from 0 to +80 kV/cm, the CTO ceramic exhibits a

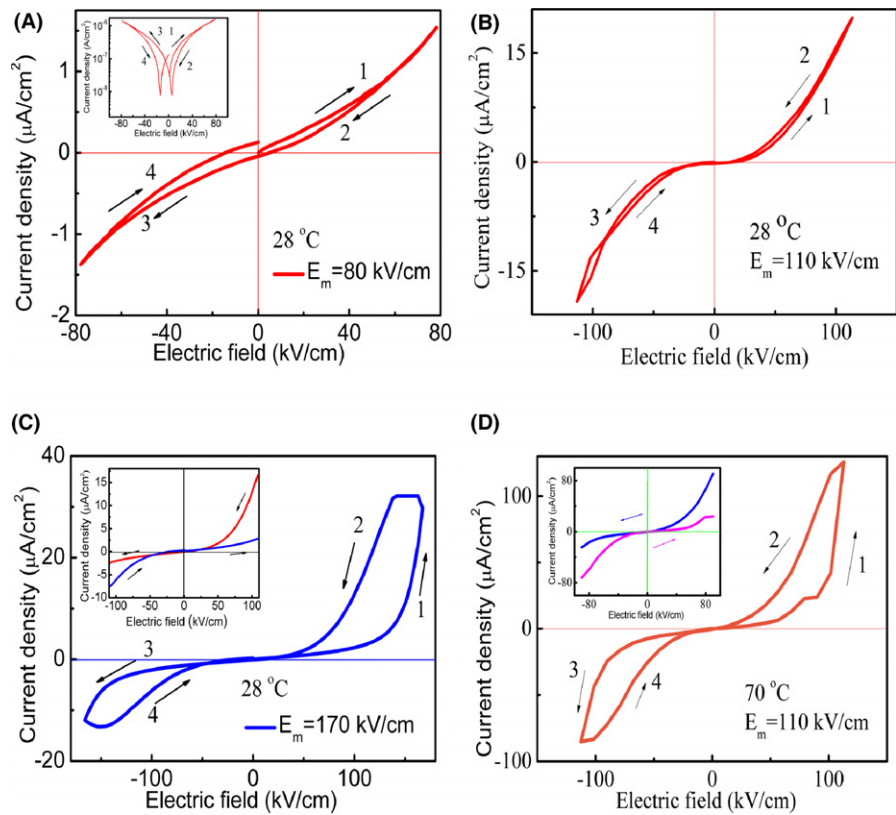


FIGURE 3 A, B and C, J - E characteristic of CTO ceramic with the maximum biased electrical field of ± 80 , ± 110 , and ± 170 kV/cm, respectively. The inset of (A) shows the same J - E curve on a semi logarithmic scale. The inset of (C) shows the sketch of the J - E curves with the maximum electric field of ± 110 kV/cm. D, J - E curves of CTO ceramic measured with maximum biased electrical field of ± 110 kV/cm at 70°C , and the lower electrical field parts are shown in the inset.[Color figure can be viewed at wileyonlinelibrary.com]

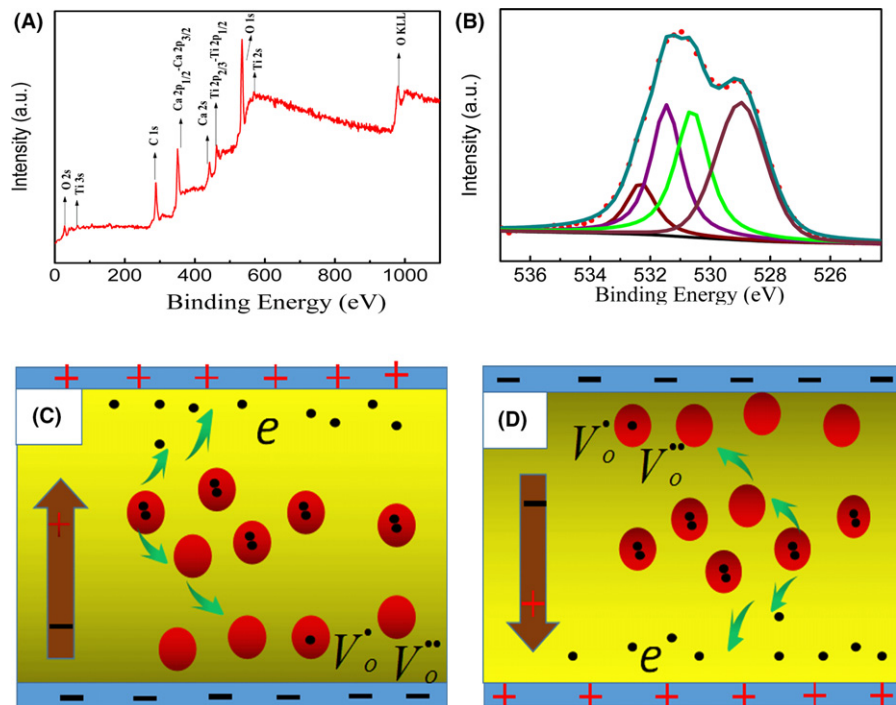


FIGURE 4 A and B, XPS survey spectra of CTO ceramic in the binding energy range of 0–1100 eV and of $O\ 1s$ core-level region, respectively. A schematic diagram to show the formation of a p-n junction-like diode with a ferroelectric polarization upward (C) or downward (D).[Color figure can be viewed at wileyonlinelibrary.com]

relatively larger leakage current than that sweeping from $+80$ to 0 kV/cm. This hysteresis behavior supposed to be the result of the ferroelectric polarization switching in CTO ceramics. It is not difficult to understand that in addition to the ohmic current contribution, some polarization switching current exists in the positive sweep regions $0 \rightarrow +80$ and 0

$\rightarrow -80$ kV/cm because of inversion of a small part of the dipole. While, since the dipole cannot inverse in the negative sweep regions $+80 \rightarrow 0$ and $-80 \rightarrow 0$ kV/cm, no polarization switching current contributes to the total amount of current.¹⁷ However, when the sweep range of electrical field is increased step by step, the J - E curve

exhibits rather different characteristics. At the beginning for the sweep range of ± 110 kV/cm, the J - E curves are still nearly symmetric but the weak hysteresis behavior disappears, as shown in Figure 3B. Then, as the sweep range of electric field reaches around ± 150 kV/cm, the hysteresis loop can be observed again but with new characteristics. With further increasing electric field range, the hysteresis becomes much wider. Figure 3C shows the representative J - E hysteresis curve probed with the sweep range of ± 170 kV/cm. The numbers labeled in the figure illustrate the sweeps sequence of biased electric field. The hysteresis loop shows an opposite trend as compared with that shown in Figure 3A. When electrical sweeping field is from 0 to $+170$ kV/cm, the samples exhibits a relatively lower leakage current than that in backward scanning process, leading to the appearance of a current hysteresis loop. In the region with negative bias, a similar hysteresis also appears in the J - E curve, indicating a resistive switching effect. Furthermore, two J - E segments (inset of Figure 3C) in the range of ± 110 kV/cm are plotted using different color solid lines. As the electrical field sweeps from 110 to -110 kV/cm, the diode-like behavior can be observed clearly, whereas for sweeping the electrical field from -110 to 110 kV/cm, the currents exhibit a reverse diode-like behavior. During a sweep cycle of biased electric field the diode polarity can be switched at about ± 110 kV/cm. In contrast, as mentioned in Figure 2B, the room-temperature P - E loops with various electric fields indicates that the CTO ceramic exhibits ferroelectricity, and its ferroelectric polarization switching occurs at the coercive field of around ± 110 kV/cm. With such bias range in the room temperature, there is no obvious hysteresis loop or resistive switching effect in J - E curve (Figure 3B), but the diode-like electric transport behavior can be observed in J - E curve at 70°C , as shown in Figure 3D, in which the electric field biased on the CTO ceramics is in the bias range of ± 110 kV/cm. Two J - E segments in the inset of Figure 3D clearly demonstrate a similar switchable diode behavior in the range of ± 90 kV/cm. Appearance of the switchable diode effect at 70°C can be ascribed to the reduced coercive electric field (~ 75 kV/cm), as shown in Figure 2E. Although the coercive field may be varied with the applied maximum electric field, the frequency of the triangle voltage excitation and temperature, the switchable diode-like J - E characteristics seems to be closely correlated with the ferroelectric polarization. I - V curves in Figure 3C and D show a clear asymmetry between positive and negative sweep regions. This asymmetry maybe due to unbalanced accumulation of oxygen vacancies and charged carriers etc.

The switchable ferroelectric diode behavior has ever been observed in BiFeO_3 single crystal.¹⁸ It was proposed that this switchable diode behavior is connected with a polarization-dependent depletion layer containing positive charged oxygen

vacancies.¹⁹ Fractions of resistance switching and rectification phenomena have been explained by bulk conduction under trap density gradient in previous report.²⁰ J - E curves with switchable rectifying characteristics was ever reported in BiFeO_3 epitaxial thin films and were explained by the polarization-modulated Schottky-like barriers.^{21,22}

The switchable diode-like J - E behavior could be ascribed to the interaction between the ferroelectric domain switching and oxygen vacancies. The electrical properties of a material are usually related with its electronic structures. In order to get electronic energy band structures of CTO, the core-level lines of constituent elements were investigated by XPS. Figure 4A presents the survey spectra of CTO ceramic in the binding energy range from 0 to 1100 eV, where the core level binding energies were aligned with respect to C 1s peak (284 eV). Photoelectron peaks and some Auger lines of constituent elements of Ca, Ti, and O elements are shown in the survey spectra. There are no other impurities existed up to 1100 eV except Carbon. The presence of oxygen vacancies is believed to be one of the main causes for the leakage current in CTO ceramics.²³ To confirm the presence of oxygen vacancies, the corresponding survey spectra of O 1s core level regions was probed with XPS and is shown in Figure 4B. Using Lorentzian–Gaussian fitting and Shirley background, the asymmetric O 1s peak can be resolved into four peaks. It is observed that the first peak locates at around 528.9 eV and can be attributed to the O^{2-} ions at the lattice sites of CTO ceramics.^{24,25} While the second peak at around 531 eV could be resolved into three peaks. The peak at the lower binding energy (530.6 eV) can be assigned to the adsorbed oxygen species.²⁶ The component at the intermediate binding energy of 531.5 eV can be assigned to the chemisorbed oxygen of the surface hydroxyl and carbonate (CO_3^{2-}).^{24,27} The highest binding energy (532.3 eV) corresponds to adsorbed water.^{26,27}

As confirmed in above-mentioned XPS O_{1s} core level profile, there are oxygen vacancies in the bulk CTO ceramics, hence, CTO ceramics can be thought as an n-type semiconductor (oxygen vacancies act as donor impurities). Figure 4C provides a schematic diagram that illustrates the formation process of a p-n junction like diode. For a CTO capacitor at low electric field, the oxygen vacancies which act as donor impurities are not easy to move or release electrons. While, under the high electric field, a neutral oxygen vacancy (V_O) would release one or two electrons so as to become positive oxygen vacancies,^{21,22} as illustrated by the following equation



The released electrons would move under the influence of the depolarization field to form an electron region near

the surface with positive bound charges. While, positive oxygen vacancies move in the opposite direction and pile up near the surface with negative bound charges. As a result, the negative electrons and positive oxygen vacancies are distributed locally unbalanced, leading to form a p - n junction like diode in the Ag/CTO/Ag capacitor, as shown in Figure 4C. This kind of junction could result in the appearance of the rectifying J - E curves (inset of Figure 3C).²⁸ When the ferroelectric polarization is reversed and point downwards, as shown in Figure 4D, the mobile charged carriers including electrons and oxygen vacancies would move and result in the redistribution in the capacitor, leading to the appearance of reverse diode-like J - E curves.

Oxygen vacancies in CTO ceramics could not only modulate the electric transportation but also modify the electronic energy band gap. The optical band properties of CTO ceramics can be described by UV-vis absorption spectrum, as presented in Figure 5A. There is a sharp increase in the wavelength range of 300–350 nm. Since CTO is a direct band gap material, as indicated from the calculated energy band structure (Figure 5B) that the minimal-energy state in the conduction band and the maximal-energy state in the valence are at the same point, the optical band gap E_g for the CTO can be calculated by the relation: $(\alpha h\nu)^2 = C(h\nu - E_g)$, where C is a constant, $h\nu$ is the photo energy and α is absorption coefficient.²⁷ The corresponding plots of $(\alpha h\nu)^2$ vs $h\nu$ for CTO sample and the value of the band gap estimated by the linear extrapolation approach are shown in the inset of Figure 5A. From intersection of the extrapolation the band gap of CTO ceramic

is estimated to be 3.27 eV. This value of band gap is much smaller than that of the single crystal (3.9 eV), due to the presence of oxygen vacancies that is in well agree with theoretical prediction.¹¹ Moreover, there is a so-called broad tail that persists to lower energies in the curve of $(\alpha h\nu)^2$ vs $h\nu$. Such a broad tail and narrowed band gap in CTO ceramic could be again ascribed to the oxygen vacancies. The presence of oxygen vacancies in CTO ceramics will raise the position of the valence band due to the overlap of the nonlocalized oxygen vacancy states and the valence band edge.^{11,29} A similar result has been found in oxygen deficient SrTiO₃.³⁰ Oxygen vacancies are thought to be able to distort the local environment around the transition-metal center, modify band width, and introduce carriers, and eventually influence the electronic properties.

In order to investigate the influence of oxygen vacancies on the electronic energy band structure of CTO, we used first-principles calculations to study the CTO's density of states (DOS) and energy band structure. The projected DOS plots for the pure CTO $2 \times 1 \times 2$ super-cell with orthorhombic structure are presented in Figure 5C. In this figure, the position of the Fermi level is located at the top of the valence band, and the valence and conduction band edges near the Fermi energy are quite sharp. It can be seen that the contribution around the bottom of conduction band is mainly from the *Ti 3d* states with a small component from the *O 2p* states. The maximal-energy state in valence band is mainly composed of the *O 2p* states with a slight contribution from *Ti 3d* orbital. This demonstrates that there is a strong hybridization between the oxygen and titanium

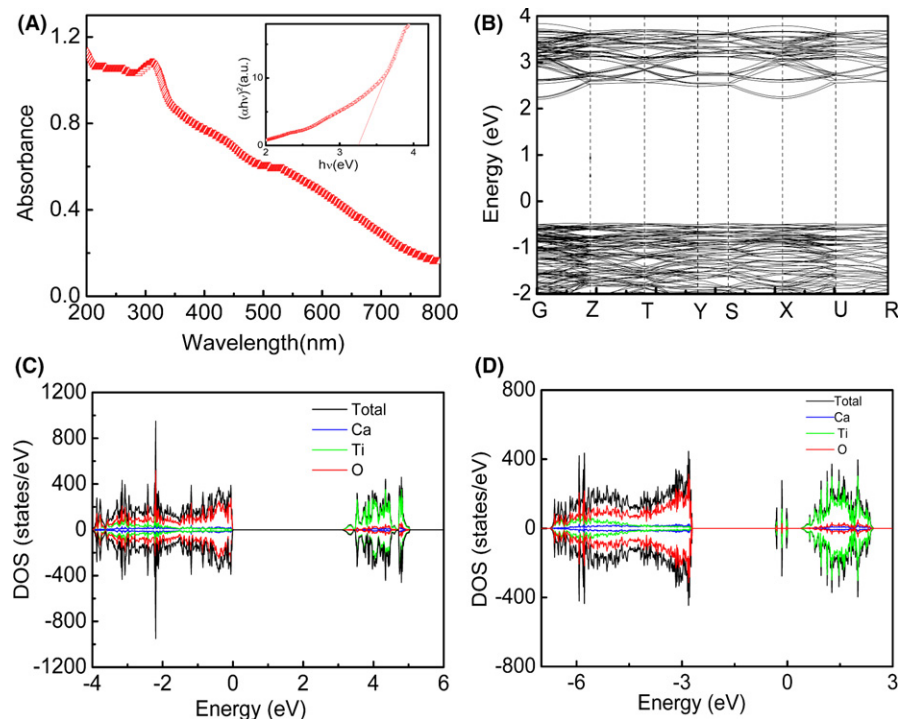


FIGURE 5 A, UV-vis absorption spectrum of CTO ceramic. The inset shows $(\alpha h\nu)^2$ vs $h\nu$ plot of CTO sample. B, The calculated electronic band structure of CTO. C and D, show the total and partial DOS of a $2 \times 1 \times 2$ CTO super-cell of pure CTO and CTO with three oxygen vacancies, respectively. [Color figure can be viewed at wileyonlinelibrary.com]

states in the CTO compound. Hence, the oxygen vacancies existing in CTO sample will dramatically influence their electronic energy band. Furthermore, it can be predicted that the photo-excitation of the electrons from the top of the valence band to bottom of the conduction band will have the effect of bringing electrons from $O\ 2p \rightarrow Ti\ 3d$ state via charge-transfer excitations.¹¹ The influence of oxygen vacancies on the electronic structure is studied via the plot of the density of states using $2 \times 1 \times 2$ super-cell CTO with three oxygen vacant sites, as shown in Figure 5D. An energy gap around 3.12 eV is found for both pure CTO and oxygen-deficient CTO samples. Such band gap value is smaller than that obtained by the optical absorption route (Figure 5A), but is generally acceptable since both local density approximation and the generalized gradient approximation based on density functional theory usually underestimate the band gap. However, the density of state curves, Figure 5D, show that by creating three oxygen vacancies in the 192-atoms super-cell of CTO, three new occupied states appear in the gap, at 2.41 eV above the top of the valence band and 0.36 eV below the bottom of the conduction band. This result is consistent with experimental estimates and theoretical prediction in strontium titanate. The presence of the defect states can facilitate the transition of carrier from the valence band to conduction band.

4 | CONCLUSIONS

To summarize, the observation of a peak in the current signal before reaching the maximum electric field indicates that domain switching is taking place in highly resistive CTO ceramics. Dynamic hysteresis measurement in CTO ceramics is reported for first time, it appears that freely movable charges contribute significantly to the electrical hysteresis loop. The switchable diode effect accompanied an abrupt jump of current in I - E curves coincides with the local switching of ferroelectric polarization. The locally unbalanced distribution of mobile charges upon application of electrical fields is thought to be the reason for the observed switchable diode effect and asymmetric J - E curves. Analysis of the linear absorption spectrum reveals a direct gap at 3.27 eV. We hope our work inspires further research on hybrid improper ferroelectricity mechanisms in other ferroelectric material.

ACKNOWLEDGMENT

This work was funded by the National Key Research and Development Program of China (2018YFB0703500), the National Natural Science Foundation of China (51572193), and the Natural Science Foundation of Tianjin (No. 17JCYBJC17600).

ORCID

Shou Yu Wang  <http://orcid.org/0000-0002-7885-3850>

REFERENCES

- Valencia S, Crassous A, Bocher L, Garcia V, Moya X, Cherifi RO, et al. Interface-induced room-temperature multiferroicity in BaTiO_3 . *Nat Mater*. 2011;10:753–8.
- Eerenstein W, Mathur ND, Scott JF. Multiferroic and magnetoelectric materials. *Nature*. 2006;442:759–65.
- Catalan G, Scott JF. Physics and applications of Bismuth Ferrite. *Adv Mater*. 2009;21:2463–85.
- Shaw TM, Trolier-McKinstry S, McIntyre PC. The properties of ferroelectric films at small dimensions. *Annu Rev Mater Sci*. 2000;30:263–98.
- Li Z, Tao K, Ma J, Gao ZP, Koval V, Jiang CJ, et al. $\text{Bi}_{3.25}\text{La}_{0.75}\text{Ti}_{2.5}\text{Nb}_{0.25}(\text{Fe}_{0.5}\text{Co}_{0.5})_{0.25}\text{O}_{12}$, a single phase room temperature multiferroic. *J Mater Chem C*. 2018;6:2733–40.
- Benedek NA, Fennie CJ. Hybrid improper ferroelectricity: a mechanism for controllable polarization-magnetization coupling. *Phys Rev Lett*. 2011;106:107204.
- Bousquet E, Dawber M, Stucki N, Lichtensteiger C, Hermet P, Gariglio S, et al. Improper ferroelectricity in perovskite oxide artificial superlattices. *Nature*. 2008;452:732–U4.
- Liu XQ, Wu JW, Shi XX, Zhao HJ, Zhou HY, Qiu RH, et al. Hybrid improper ferroelectricity in Ruddlesden-Popper $\text{Ca}_3(\text{Ti}, \text{Mn})_2\text{O}_7$ ceramics. *Appl Phys Lett*. 2015;106:202903.
- Benedek NA, Mulder AT, Fennie CJ. Polar octahedral rotations: a path to new multifunctional materials. *J Solid State Chem*. 2012;195:11–20.
- Oh YS, Luo X, Huang FT, Wang YZ, Cheong SW. Experimental demonstration of hybrid improper ferroelectricity and the presence of abundant charged walls in $(\text{Ca}, \text{Sr})_3\text{Ti}_2\text{O}_7$ crystals. *Nat Mater*. 2015;14:407–13.
- Cherian JG, Birol T, Harms NC, Gao B, Cheong SW, Vanderbilt D, et al. Optical spectroscopy and band gap analysis of hybrid improper ferroelectric $\text{Ca}_3\text{Ti}_2\text{O}_7$. *Appl Phys Lett*. 2016;108:262901.
- Nowadnick EA, Fennie CJ. Domains and ferroelectric switching pathways in $\text{Ca}_3\text{Ti}_2\text{O}_7$ from first principles. *Phys Rev B*. 2016;94:104105.
- Huang FT, Xue F, Gao B, Wang LH, Luo X, Cai W, et al. Domain topology and domain switching kinetics in a hybrid improper ferroelectric. *Nat Commun*. 2016;7:11602.
- Li X, Yang L, Li CF, Liu MF, Fan Z, Xie YL, et al. Ultra-low coercive field of improper ferroelectric $\text{Ca}_3\text{Ti}_2\text{O}_7$ epitaxial thin films. *Appl Phys Lett*. 2017;110:042901.
- Cao RP, Chen G, Yu XG, Cao CY, Chen KB, Liu P, et al. Luminescence properties of $\text{Ca}_3\text{Ti}_2\text{O}_7:\text{Eu}^{3+}$, Bi^{3+} , R^{3+} ($\text{R}^{3+} = \text{Li}^+$, Na^+ , and K^+) red emission phosphor. *J Solid State Chem*. 2014;220:97–101.
- Yan HX, Inam F, Viola G, Ning HP, Zhang HT, Jiang QH, et al. The contribution of electrical conductivity, dielectric permittivity and domain switching in Ferroelectric Hysteresis Loops. *J Adv Dielect*. 2011;1:107–18.
- Yan F, Xing GZ, Li L. Low temperature dependent ferroelectric resistive switching in epitaxial BiFeO_3 films. *Appl Phys Lett*. 2014;104:132904.

18. Choi T, Lee S, Choi YJ, Kiryukhin V, Cheong SW. Switchable ferroelectric diode and photovoltaic effect in BiFeO₃. *Science*. 2009;324:63–6.
19. Yuan GL, Wang JL. Evidences for the depletion region induced by the polarization of ferroelectric semiconductors. *Appl Phys Lett*. 2009;95:252904.
20. Watanabe Y. Unidirectional bulk conduction and the anomalous temperature dependence of drift current under a trap-density gradient. *Phys Rev B*. 2010;81:195210.
21. Wang C, Jin KJ, Xu ZT, Wang L, Ge C, Lu HB, et al. Switchable diode effect and ferroelectric resistive switching in epitaxial BiFeO₃ thin films. *Appl Phys Lett*. 2011;98:192901.
22. Yang CH, Seidel J, Kim SY, Rossen PB, Yu P, Gajek M, et al. Electric modulation of conduction in multiferroic Ca-doped BiFeO₃ films. *Nat Mater*. 2009;8:485–93.
23. Han YL, Liu WF, Xu XL, Guo MC, Zhang XN, Wu P, et al. The abnormal optical property and room-temperature exchange bias behavior in Na- and Ru-codoped BiFeO₃ nanoparticles. *J Am Ceram Soc*. 2016;99:3616–22.
24. Fang L, Liu JA, Ju S, Zheng FG, Dong W, Shen MR. Experimental and theoretical evidence of enhanced ferromagnetism in sonochemical synthesized BiFeO₃ nanoparticles. *Appl Phys Lett*. 2010;97:242501.
25. Wang X, Hu GD, Cheng L, Yang CH, Wu WB. Comparative study on aging effect in BiFeO₃ thin films substituted at A- and B-sites. *Appl Phys Lett*. 2011;99:262901.
26. Sutthiumporn K, Kawi S. Promotional effect of alkaline earth over Ni–La₂O₃ catalyst for CO₂ reforming of CH₄: role of surface oxygen species on H₂ production and carbon suppression. *Int J Hydrog Energy*. 2011;36:14435–46.
27. Zhang XN, Liu WF, Han YL, Huang C, Wu P, Zhou W, et al. Novel optical and magnetic properties of Li-doped quasi-2D manganate Ca₃Mn₂O₇ particles. *J Mater Chem C*. 2017;5:7011–9.
28. Wang SY, Liu WF, Gao J, Qiu X, Feng Y, Hou GX, et al. Resistive switching and threshold switching behaviors in La_{0.1}Bi_{0.9}Fe_{1-x}Co_xO₃ ceramics. *J Appl Phys*. 2012;112:034110.
29. Liu HY, Zeng F, Lin YS, Wang GY, Pan F. Correlation of oxygen vacancy variations to band gap changes in epitaxial ZnO thin films. *Appl Phys Lett*. 2013;102:181908.
30. Orhan E, Pontes FM, Santos MA, Leite ER, Beltran A, Andres J, et al. Combined experimental and theoretical study to understand the photoluminescence of Sr_{1-x}TiO_{3-x}. *J Phys Chem B*. 2004;108:9221–7.

How to cite this article: Tong BY, Wang SY, Wong-Ng W, et al. Polarization switching dynamics and switchable diode effect in hybrid improper ferroelectric Ca₃Ti₂O₇ ceramics. *J Am Ceram Soc*. 2019;102:1875–1883. <https://doi.org/10.1111/jace.16077>